Inorg. Chem. **2007**, *46*, 6668–6674

Synthesis and Structural and Magnetic Characterization of $\{[(phen)_2Ni]_2(\mu\text{-}P_2O_7)\}\cdot 27H_2O$ and $\{[(phen)_2Mn]_2(\mu\text{-}P_2O_7)\}\cdot 13H_2O$: Rare Examples of Coordination Complexes with the Pyrophosphate Ligand

Oluwatayo F. Ikotun,[†] N. Gabriel Armatus,[†] Miguel Julve,*[,‡] Paul E. Kruger,*[,§] Francesc Lloret,[‡] Mark Nieuwenhuyzen,[||] and Robert P. Doyle*[,†]

Department of Chemistry, Syracuse University, Syracuse, New York 13244-4100, Department of Química Inorgánica/Instituto de Ciencia Molecular, Universitat de Valencia, Polígono La Coma s/n, E-46980 Paterna, Valencia, Spain, Department of Chemistry, College of Science, University of Canterbury, Christchurch, 8020, New Zealand, and Chemistry Department, The Queen's University of Belfast, Belfast, U.K., BT9 5AG

Received March 7, 2007

The reaction in water of M(II) [M = Ni or Mn] with 1,10-phenanthroline (phen) and sodium pyrophosphate ($Na_4P_2O_7$) in a 2:4:1 stoichiometry resulted in the crystallization of dinuclear complexes featuring the heretofore rare bridging pyrophosphate. Single-crystal X-ray diffraction studies revealed the complexes to be $\{[(phen)_2Ni]_2(\mu\text{-}P_2O_7)\}\cdot 27H_2O$ (**1**) and $\{[(phen)_2Mn]_2(\mu\text{-}P_2O_7)\}\cdot 13H_2O$ (**2**) where the asymmetric $M(phen)_2$ units are bridged by bis-bidentate pyrophosphate, each metal ion exhibiting a distorted octahedral geometry. The bridging pyrophosphate places adjacent metal centers at 5.031 Å in **1** and 4.700 Å in **2**, and its conformation also gives rise to an intramolecular π–π interaction between two adjacent phen ligands. Intermolecular π–π interactions between phen ligands from adjacent dinuclear complexes create an ornate 3D network in **1**, whereas a 2D sheet results in **2**. The hydrophilic nature of the pyrophosphate ligand leads to heavy hydration with the potential solvent-accessible area for **1** and **2** accounting for 45.7% and 26.4% of their unit cell volumes, respectively. Variable-temperature magnetic susceptibility measurements on polycrystalline samples of **1** and **2** revealed net weak intramolecular antiferromagnetic coupling between metal centers in both compounds with $J = -3.77$ cm^{-1} in **1** and $J = -0.88$ cm^{-1} in **2**, the Hamiltonian being defined as $H = -JS_A\cdot S_B$. The ability of the bis-bidentate pyrophosphate to mediate magnetic interactions between divalent first row transition metal ions is discussed bearing in mind the number and nature of the interacting magnetic orbitals.

Introduction

The role of diphosphate, more commonly known as pyrophosphate ($P_2O_7^{4-}$), in biological systems has long been of interest to chemists. Pyrophosphate is ubiquitous in nature, involved in processes such as oxidative phosphorylation,[1] oxidative decarboxylation (e.g., thiamin pyrophosphate, vitamin B_1),[2] energy storage, and energy transduction.[3] Calcium pyrophosphate build-up in joints is the cause of a form of chronic rheumatoid arthritis[4] and certain pyrophosphatases (e.g., from the yeast *Saccharomyces cerevisiae*) are dependent on magnesium or manganese for function.[5] Indeed, these enzymes can have as many as four functional divalent metal ions in the active site, with two metal ions bound as

* To whom correspondence should be addressed. E-mail: rpdoyle@syr.edu.
[†] Syracuse University.
[‡] Universitat de Valencia.
[§] University of Canterbury.
[||] The Queen's University of Belfast.

(1) (a) Walker, J. E. *Angew. Chem.* **1998**, *110*, 2438. (b) Walker, J. E. *Angew. Chem., Int. Ed.* **1998**, *37*, 2308. (c) Boyer, P. D. *Angew. Chem.* **1998**, *110*, 2424. (d) Boyer, P. D. *Angew. Chem., Int. Ed.* **1998**, *37*, 2296.
(2) Dorrestein, P. C.; Zhai, H.; Taylor, S. V.; McLafferty, F. W.; Begley, T. P. *Biochemistry* **2003**, 42, 12430.
(3) (a) *The Biochemistry of Nucleic Acids*, 10th ed.; Adams, R. L. P., Knowler, J. T., Leader, D. P., Eds.; Chapman and Hall: New York, 1986. (b) *Nucleic Acids in Chemistry and Biology*, 2nd ed.; Blackburn, G. M., Gait, M. J., Eds.; Oxford University Press: New York, 1996. (c) Berg, J. M.; Tymoczko, J. L.; Stryer, L. *Biochemistry*, 5th ed.; W. H. Freeman and Company: New York, 2001.
(4) Ea, H. K.; Liote, F. *Curr. Rheumatol. Rep.* **2004**, *6* (3), 221.
(5) (a) Harutyunyan, E. H.; Kuranova, I. P.; Vainshtein, B. K.; Hohne, W. E.; Lamzin, V. S.; Dauter, Z.; Teplyakov, A. V.; Wilson, K. S. *Eur. J. Biochem.* **1996**, *239* (1), 220. (b) Gomez-Garcia, M. R.; Losada, M.; Serrano, A. *Biochem. J.* **2006**, *395* (1), 211.

10.1021/ic700439a CCC: $37.00
Published on Web 07/17/2007

Table 1. Structurally Characterized Multinuclear Coordination Complexes Featuring the Pyrophosphate Ligand[a]

metal ion	compound	space group	ref
Cu(II)	[(CuL)$_4$(μ-P$_2$O$_7$)]·nH$_2$O	$C2/c$	10
Cu(II)	{[(bipy)Cu(H$_2$O)]$_2$(μ_4-P$_2$O$_7$)·7H$_2$O}	$P\bar{1}$	11
Co(II)	{[Co(tpa)]$_2$(μ-P$_2$O$_7$)·(ClO$_4$)$_2$]·2.5H$_2$O·2.5CH$_3$OH}	$P1$	12
Cu(II)	{[(bipy)Cu(H$_2$O)(μ-P$_2$O$_7$)Na$_2$(H$_2$O)$_6$]·4H$_2$O}	$P1$	13
Zn(II)	{[(bipy)Zn(H$_2$O)(μ-P$_2$O$_7$)Zn(bipy)]$_2$·14H$_2$O}	$P2_1/c$	13
V(IV)	[(tmp)$_4$[(VO)$_4$(μ-P$_2$O$_7$)$_2$(OCH$_3$)$_4$]	$P2_1/n$	14

[a] Abbreviations: n = 9−12; L = 2-formylpyridine thiosemicarbazone; bipy = 2,2′-bipyridine; tpa = tris(2-pyridylmethyl)amine; tmp = 2,4,6-trimethylpyridine.

essential cofactors, whereas the third and fourth are ligated to pyrophosphate/phosphate forming substrate/product motifs.[5] Outside of biology, inorganic pyrophosphate salts have drawn interest as promising materials for laser hosts, in ceramics, electric, magnetic, and catalytic applications.[6] A vanadium pyrophosphate-based system is an important heterogeneous/contact catalyst, being the only example of a heterogeneous catalyst used in the selective oxidation of alkanes (e.g., the conversion of butane to maleic anhydride).[7] The multidentate nature of pyrophosphate makes it an attractive ligand for the potential formation of multinuclear complexes with varied structural types and properties. However, despite the diversity and importance of pyrophosphate interactions with metal ions, it is surprising to note that the coordination chemistry of pyrophosphate remains virtually unexplored. A review of the Cambridge Crystallographic Database revealed only six such complexes (see Table 1).[8] The dearth of structurally characterized pyrophosphate complexes possibly arises as a consequence of its sensitivity to hydrolysis especially in the presence of divalent metal ions.[9]

The few examples listed in Table 1 demonstrate the ability of the pyrophosphate tetra-anion to act as a structurally flexible bridging unit to produce a variety of complexes with variable nuclearity. Given the scarcity of such structures, the dearth of magnetic characterization and the relevance of pyrophosphate to both biology and materials science, we have focused some recent efforts on using pyrophosphate in the synthesis of coordination complexes and investigating the structures, as well as the magnetic and catalytic properties of the species obtained.[11,13] Our success to date is in part due to our strategy of preventing hydrolysis of pyrophosphate during synthesis. This is achieved by using previously chelated metal ions, e.g., 'M(II)−phen' species (phen 1,10-phenanthroline), as precursors since short-chain polyphosphates have been shown to be fairly inert to hydrolysis in the presence of chelated metal ions (Table 1). We report herein the synthesis and structural, magnetic, and thermal characterization of two pyrophosphate-bridged dinuclear species of formula {[(phen)$_4$(Ni)$_2$(μ_4-P$_2$O$_7$)]·27H$_2$O} (**1**) and {[(phen)$_4$(Mn)$_2$(μ_4-P$_2$O$_7$)]·13H$_2$O} (**2**). They are the first such examples of Ni(II) and Mn(II) complexes incorporating the pyrophosphate ligand. From the structural studies, it is evident that **1** and **2** crystallize with a high degree of hydration and, in the case of **1**, an ornate set of channels runs through the structure. The nature of these channels and the magnetic behavior of **1** and **2** are discussed.

Experimental Section

Solvents and chemicals were of laboratory grade and were used as received. Electrospray mass spectrometry was performed on a Shimadzu LCMS-2010 A system at a cone voltage of 5 kV. Infrared spectra were recorded on a Nicolet Magna-IR 850 Series II spectrophotometer as KBr pellets. Thermal analysis was performed on a TA instrument TGA Q500 using 2−6 mg samples placed on platinum pans and run under a nitrogen atmosphere (40 mL/min). The temperature was ramped from ∼25 to 500 °C at a rate of 10 °C/min. Analyses were performed using the TA instruments Universal Analysis 2000 software program. Elemental analysis (C, H, N, P) was performed by Quantitative Technologies, Inc., Whitehouse, NJ. Water was distilled and deionized to 18.6 MΩ using a Barnstead Diamond RO reverse osmosis machine coupled to a Barnstead Nano Diamond ultrapurification machine. Variable-temperature magnetic susceptibility measurements were performed on a Quantum design SQUID susceptometer in the temperature range 1.9−300 K with an applied magnetic field of H = 1000 G ($T \geq$ 100 K) and 250 G ($T <$ 100 K). Crystalline samples (typically 40 mg) were obtained directly from the reaction mixture, air-dried, and powdered in a mortar. Diamagnetic corrections for the constituent atoms were estimated using Pascal's constants, and corrections for the sample holder and the temperature-independent paramagnetism were also performed. Corrections for the temperature-independent magnetism (diamagnetic contribution of the constituent atoms plus temperature-independent paramagnetism of the metal ions) of **1** and **2** were considered as variable parameters in the fit, and the values for two metal ions are -500×10^{-6} cm^3/mol for **1** and -620×10^{-6} cm^3/mol for **2**. They are as expected for the chemical compositions. Corrections for the sample holder were also applied. Electronic absorption spectra were obtained on a Varian Cary 50 Bio spectrophotometer in 1 mL Quartz cuvettes (Sigma) between 200 and 800 nm at ambient temperature.

Synthesis of 1. Nickel chloride (0.60 g, 2.5 mmol) was dissolved in 25 mL of distilled water. To this was added a water/ethanol (40:60, 25 mL) solution of 1,10-phenanthroline (0.91 g, 5 mmol), resulting in a light-purple-colored solution after ca. 10 min. Solid sodium pyrophosphate (0.33 g, 1.25 mmol) was added directly, and

(6) (a) Kasuga, T.; Terada, M.; Nogamin, M.; Niinomi, M. *J. Mater. Res.* **2001**, *16*, 876. (b) Wilson, S. T.; Lok, B. M., Messian, C. A., Cannon, T. R., Flanigen, E.M. *J. Am. Chem. Soc*., **1982**, *104*, 1146. (c) Thomas, J. M. *Angew. Chem., Int. Ed*, **1994**, *106*, 963. (d) Hartmann, M., Kevan, L., *Chem. Mater* **1999**, 99, 635. (d) Sun, X.; Xu, X.-G.; Fu, Y.-J.; Wang, S.-L.; Zeng, H.; Li, Y.-P. *Cryst. Res. Technol*. **2001**, 4−5, 465.
(7) (a) Guliants, V. V.; Holmes, S. A.; Benziger, J. B.; Heany, P.; Yates, D.; Wachs, I. E. *J. Mol. Catal. A* **2001**, *172*, 265. (b) Toradi, C. C.; Calabres, J. C. *Inorg. Chem*. **1984**, *23*, 1308. (c) Centri, G.; Trifiro, F. E., J. R.; Franchetti, V. M. *Chem. Rev.* **1988**, *88*, 55.
(8) Search was conducted through the Cambridge Structural Database (www.ccdc.cam.ac.uk) using ConQuest search and retrieval software.
(9) (a) Heikinheimo, P.; Tuominen, V.; Ahonen, A. -K.; Teplyakov, A.; Cooperman, B.S.; Baykov, A.A.; Lahti, R.; Goldman, A. *Proc. Natl. Acad. Sci. U.S.A.* **2001**, *98*, 3121. (b) Zyryanov, A. B.; Shestakov, A. S.; Lahti, R.; Baykov, A. A. *Biochem. J*. **2002**, *367*, 901.
(10) Ainscough, E. W.; Brodie, A. M.; Ranford, J. D.; Waters, J. M.; Murray, K. S. *Inorg. Chim. Acta* **1992**, *197*, 107.
(11) Kruger, P. E.; Doyle, R. P.; Julve, M.; Lloret, F.; Niewenhuyzen, M. *Inorg. Chem*. **2001**, *40*, 1726.
(12) Funshashi, Y.; Yoneda, A.; Taki, C.; Kosuge, M.; Ozawa, T.; Jitsukawa, K.; Masuda, H. *Chem. Lett*. **2005**, *34*, 1332.
(13) Doyle, R. P.; Niewenhuyzen, M.; Kruger, P. E. *Dalton Trans.* **2005**, 3745.
(14) Herron, N.; Thorn, D. I.; Harlow, R. L.; Coulston, G. W. *J. Am. Chem. Soc.* **1997**, *119*, 7149.

the mixture was allowed to stir for an additional hour. The purple solution that resulted was minimized in vacuo (to ~10% of initial volume) and passed through a 45 μm filter (Fisher). Crystallization was conducted by slow evaporation of the solvent under ambient conditions. A mixture of blue rods and block crystals were formed after 1 day. They were removed by filtering in vacuo, and the solution was again allowed to stand at room temperature. Only the blue, block-shaped crystals subsequently evolved from the solution over ca. 1 week. Found: C, 46.53; H, 4.84; N, 8.58; P, 4.98%. $Ni_2P_2O_{19}N_8H_{56}C_{48}$ (vacuum-dried; 12 waters of crystallization remain; see Thermal Analysis) requires: C, 46.93; H, 4.59; N, 8.62; P, 5.04%. IR (KBr): 3399br, 1625m, 1516s, 1424s, 1142w, 1103w, 846s, 725s cm^{-1}. MS (ESI): 594.8 *m*/*z*. UV−vis (50:50 v/v H_2O/EtOH): λ_{max}/nm 604 (17.24 M^{-1} cm^{-1}).

Synthesis of 2. An aqueous suspension of phen (0.91 g, 5 mmol) was added to an aqueous solution of manganese(II) chloride (0.49 g, 2.5 mmol) with stirring at room temperature. A pale yellow solution resulted after ca. 15 min. Following the addition of solid sodium pyrophosphate (0.33 g, 1.25 mmol), a yellow precipitate was observed. As this precipitate was insoluble in any solvent tested, the reaction above was repeated in a H-tube in an attempt to get crystals suitable for X-ray diffraction studies. Briefly, one arm of the tube contained an aqueous solution of manganese(II) chloride (10 mM) and phen (20 mM), whereas an aqueous solution of sodium pyrophosphate (5 mM) was introduced in the other arm. The tubes of both arms were filled by slow addition of water until they mixed across the H-tube bridge and the setup was then allowed to stand, sealed, at room temperature. Compound **2** was obtained as small yellow crystalline blocks over ca. 1 month. Found: C, 50.21; H, 4.14; N, 9.54% $Mn_2P_2O_{15}N_8H_{48}C_{48}$ (vacuum-dried, 8 waters of crystallization remaining) requires C, 50.18; H, 4.21; N, 9.75%. IR (KBr): 1510m, 1424s, 1384w, 1342w, 1138br, 1082s, 881m, 848m, 731s cm^{-1}.

Structure Determination and Refinement of 1 and 2. Structural measurements were performed on a Bruker-AXS SMART-CCD diffractometer at low temperature (90 K) using graphite-monochromated Mo Kα radiation (λ = 0.71073 Å). Absorption corrections were applied using SADABS and SHELXTL.[15] The structures were solved using direct methods and refined using the SHELXTL program package.[16] All non-hydrogen atoms, except those exhibiting disorder, were refined anistropically. Aromatic hydrogen atoms were assigned to calculated positions and refined using a riding model. Due to the high degree of hydration and disorder, hydrogen atoms could not be located for the water molecules in **1**. Key crystallographic data are given in Table 2. Crystallographic data (CIF file) for complexes **1** and **2** have been deposited with the Cambridge Crystallographic Data Centre, CCDC No 638729 and 637920, respectively. Copies of this information may be obtained free of charge from the Director, CCDC, 12 Union Road, Cambridge, CB2 1EZ, UK (Fax + 44 1223 336 033; email: deposit@ccdc.cam.ac.uk or via the Internet www.ccdc.cam.ac.uk.

Results and Discussion

Synthesis and Characterization of 1. Compound **1** was synthesized from an aqueous suspension of nickel(II) chloride hexahydrate, phen, and sodium pyrophosphate in a stoichiometric ratio of 2:4:1 to give a purple solution that yielded blue crystalline rods and blocks upon standing over several days. Block-shaped crystals were separated by filtering the mother liquor and leaving the filtrate to stand over 6 days. The infrared spectrum of the block crystals indicated the presence of pyrophosphate with characteristic [P−O−P] stretches observed at 1103 and 845 cm^{-1}.[17] Bands due to the phen ligand were observed at 1515 and 1424 cm^{-1}. A strong broad band at 3339 cm^{-1} and a weak band at 1625 cm^{-1} were indicative of the presence of water molecules of crystallization. Microanalytical data (C, H, N, P) were consistent with the following formulation $[(phen)_4(Ni)_2(\mu\text{-}P_2O_7)]\cdot 12H_2O$, and ESI mass spectrometry performed upon aqueous solutions gave a parent ion centered at $m/z = 594.85$, which equates to $[(phen)_2Ni(H_3P_2O_7)]^+$. The d−d spectra of aqueous solutions exhibited a very broad and featureless band centered at 604 nm (17.24 M^{-1} cm^{-1}), which is consistent with the presence of a Ni(II) chromophore with distorted octahedral geometry.[18] This was proved through a single-crystal X-ray crystal diffraction study.

Attempts to obtain a structure of the blue rods were unsuccessful. Given that these crystals disappear in mother liquor over a few days and that they are not obtained at lower solution concentrations, most likely they are an unstable kinetic product, the block-shaped crystals of **1** being the more stable thermodynamic product. Pink crystals of the tris-chelated species $[Ni(phen)_3(Cl_2)]$ were also observed with any excess of the phen ligand.

Crystal Structure of 1. The atomic numbering scheme and atom connectivity for **1** are shown in Figure 1. **1** crystallizes in the tetragonal $I4_1/acd$ space group. The molecular structure of **1** is comprised of neutral $\{[(phen)_2(Ni)]_2(\mu\text{-}P_2O_7)\}$ dinuclear nickel(II) units with two crystallographically unique nickel atoms [Ni(I) and Ni(2)] in a distorted octahedral geometry. Selected bond lengths and angles for **1** are brought together in Table 3. The N_4O_2 coordination chromophore about each nickel atom is irregular and derived from four nitrogen atoms from two phen ligands

Table 2. Crystallographic Details for **1** and **2**

	1	**2**
chemical formula	$C_{49}H_{89}Ni_2N_8O_{34}P_2$	$C_{48}H_{58}Mn_2N_8O_{20}P_2$
fw	1513.5981	1238.84
cryst syst	tetragonal	triclinic
space group	$I4_1/acd$	$P\bar{1}$
μ (Mo Kα, mm^{-1})	6.302	0.606
a/Å	42.965(8)	13.693(3)
b/Å	42.965(8)	14.093(3)
c/Å	29.386(2)	14.602(3)
α/°	90.0	89.962(5)
β/°	90.0	77.079(5)
γ/°	90.0	82.916(5)
V/Å^3	54248.7(1)	2724.5(10)
Z	32	2
D_c/g cm^{-3}	1.485	1.510
θ_{max}	22.50	28.28
R1, wR2 [$I > 2\sigma(I)$]	0.1081, 0.2842	0.0747, 0.1662
R1, wR2 (all data)	0.1662, 0.3538	0.1176, 0.1875
reflns collected	8880	28 966
reflns observed	5330	13 434

(15) Sheldrick, G. M. *SHELXTL Version 5.0, A System for Structure Solution and Refinement*; Bruker-AXS: Madison, WI, 1998.
(16) *SHELXTL PC, version 6.1*; Bruker-AXS, Inc.: Madison, WI, 2002.
(17) Nakamoto, K. *Infrared and Raman Spectra of Inorganic and Coordination Compounds, Part B, Applications in Coordination, Organometallics and Bioinorganic Chemistry*, 5th ed.; Wiley: Chichester, 1997.
(18) Cotton, F. A.; Wilkinson, G. *Advanced Inorganic Chemistry*, 5th ed.; Wiley: New York, 1999.

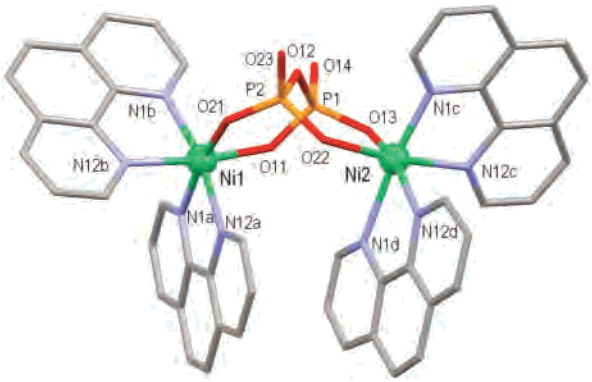

Figure 1. Molecular structure of **1** with the atom numbering. Hydrogen atoms, the disordered phen ligand, and the water molecules of crystallization have been removed for clarity.

Table 3. Selected Bond Lengths (Å) and Angles (deg) for **1**

Ni(1)−O(11)	2.051(8)	Ni(2)−O(22)	2.097(9)
Ni(1)−O(21)	2.045(7)	Ni(2)−N(1c)	2.048(13)
Ni(1)−N(1a)	2.106(8)	Ni(2)−N(1d)	2.327(19)
Ni(1)−N(1b)	2.127(8)	NI(2)- N(12c)	2.110(10)
Ni(1)−N(12a)	2.105(8)	P(2)−O(12)	1.568(10)
Ni(1)−N(12b)	2.095(11)	P(2)−O(23)	1.497(9)
Ni(2)−N(12d)	2.245(17)	P(1)−O(14)	1.432(8)
Ni(2)−O(13)	2.038(7)	P(1)−O(12)	1.667(9)
N(12b)−Ni(1)−N(1a)	92.5(3)	N(1d)−Ni(2)−N(12d)	72.0(6)
Ni(2)−O(13)−P(1)	125.95(5)	O(13)−Ni(2)−O(22)	92.3(3)
N(12b)−Ni(1)−(O11)	170.29(3)	O(13)−Ni(2)−N(12d)	161.8(5)
N(1)−Ni(1)−(N1a)	79.0(3)	O(13)−Ni(2)−N(1c)	97.3(4)
O(11)−Ni(1)−(O21)	93.74(3)	O(11)−P(1)−O(13)	111.99(4)
N(12a) --Ni(1)−N(1a)	78.9(3)	P(1)−O(12)−P(2)	124.8(5)
O(21)−Ni(1)−N(12a)	90.1(3)	O(21)−P(2)−O(22)	114.6(5)
O(22)−Ni(2)−N(12c)	172.02(4)	Ni(1)−O(11)−P(1)	131.13(4)
N(12c)−Ni(2)−N(12d)	92.1(6)	Ni(1)−O(21)−P(2)	126.23(5)
N(1c)−Ni(2)−N(12c)	80.1(5)	O(21)−Ni(1)−N(1a)	168.9(3)

and two oxygen atoms from the bridging pyrophosphate ligand. The pyrophosphate group adopts the bis-bidentate coordination mode subtending a six-membered chelate ring at each nickel atom. The nickel−nickel distance across the pyrophosphate bridge is 5.031 Å. The best equatorial plane about Ni(1) is defined by the [O11−O21−N1a−N12b] donor set (dihedral angle is 20.6°) with Ni(1) displaced 0.013 Å from the mean plane. For Ni(2), the best equatorial plane is defined by the [O13−O22−N12c−N12d] donor set (dihedral angle is 4.84°) with Ni(2) displaced 0.081 Å from the mean plane. Terminal P═O bonds lengths in the bridging pyrophosphate (1.432 [P(1)−O(14)] and 1.497 Å [P(2)−O(23)]) are shorter than those of the inner P−O bonds, which range between 1.515 [P(2)−O(22)] and 1.667 Å [P(1)−O(12)], consistent with their double- and single-bond character. Two phen ligands at Ni(1) [N(1a)/N(12a)] and Ni(2) [(N(1d)/N(12d)] interact with each other via an intramolecular face-to-face $\pi-\pi$ interaction with a separation at closest contact of 3.10 Å, and this interaction flanks the bridging pyrophosphate ligand, (see Figure 1). The phen ligands about Ni(1) and Ni(2) also interact with adjacent phen ligands through intermolecular offset face-to-face $\pi-\pi$ interactions with dihedral angles between adjacent rings of 3.8−6.0° and separations at closest contact ranging from 3.42 to 3.50 Å. In addition, edge-to-face intermolecular interactions are also evident between some adjacent phen ligands. These interactions form a 3D network, and they lead to the formation of

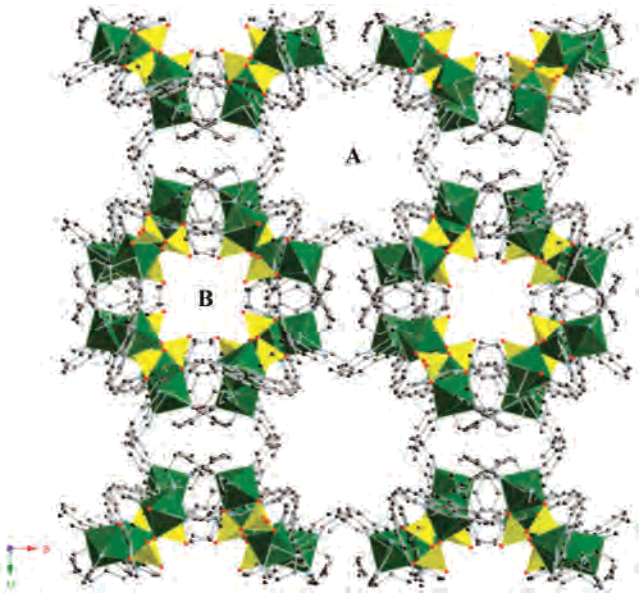

Figure 2. Packing diagram of **1** looking down the crystallographic *c* axis. The dimensions of channels **A** and **B** are 17.813 × 17.813 and 13.163 × 15.71 Å^2, respectively. Hydrogen atoms and lattice water molecules have been omitted for clarity.

channels that run down the crystallographic *c* axis and within which the lattice water molecules reside (see Figures 2 and S2). These channels constitute a potential solvent-accessible area of 45.7% of the crystal.[19]

The dimensions of the **A** and **B** channels are 17.813 × 17.813 and 13.163 × 15.709 Å^2, respectively. The **A** channel is lined predominantly by phen ligands with aromatic C−H groups projecting into it giving it a hydrophobic lining, whereas the **B** channel is lined predominantly by the hydrophilic pyrophosphate ligand with the terminal (and uncoordinated) P═O group projecting into it, as shown in Figure 2 (see also Figures S1 and S2)

Synthesis and Characterization of 2. An aqueous solution of manganese(II) chloride tetrahydrate was reacted with an aqueous suspension of phen with a 1:2 Mn(II)-to-phen molar ratio. A clear yellow solution resulted upon stirring at room temperature. A yellow precipitate formed immediately upon addition of a 0.5 stoichiometric equivalent [based on Mn(II)] of sodium pyrophosphate. This precipitate proved to be insoluble in any solvent tested. So, slow diffusion of the starting materials in a H-tube was used to acquire single crystals of **2** suitable for X-ray diffraction studies. Infrared spectroscopy indicated the presence of characteristic phen (1510 and 1424 cm^{-1}) and pyrophosphate (1138 and 848 cm^{-1}) absorption peaks. Elemental analyses (C, H, N, P) were consistent with the formation of a dinuclear Mn(II) complex with the following formulation {[(phen)$_4$-(Mn)$_2$(μ-P$_2$O$_7$)]·8H$_2$O}. The single-crystal X-ray crystal diffraction study confirmed its dinuclear nature.

Crystal Structure of 2. The atomic numbering scheme and atom connectivity for **2** are shown in Figure 3. The dinuclear unit is made up of two crystallographically

(19) Spek, A. L. *PLATON, A Multipurpose Crystallographic Tool*; Utrecht University: Utrecht, The Netherlands, 2000. *Mercury 1.1*; CCDC: Cambridge 2002.

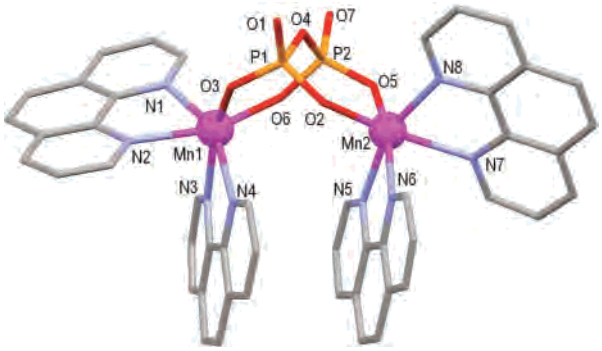

Figure 3. Molecular structure of **2** showing the atomic-labeling scheme. The hydrogen atoms and the water molecules of crystallization are omitted for clarity.

Table 4. Selected Bond Lengths (Å) and Angles (deg) for **2**

Mn(1)−O(3)	2.083(3)	Mn(2)−N(6)	2.273(4)
Mn(1)−O(6)	2.146(3)	Mn(2)−O(2)	2.096(3)
Mn(1)−N(1)	2.294(3)	Mn(2)−N(7)	2.342(4)
Mn(1)−N(4)	2.310(4)	Mn(2)−N(5)	2.274(4)
Mn(1)−N(2)	2.324(4)	P(1)−O(1)	1.504(3)
Mn(1)−N(3)	2.334(4)	P(1)−O(4)	1.627(3)
Mn(2)−O(5)	2.095(3)	P(2)−O(4)	1.613(3)
Mn(2)−N(8)	2.257(4)	P(2)−O(7)	1.514(3)
Mn(1)−O(3)−P(1)	126.85(17)	O(5)−P(2)−O(6)	111.65(17)
O(3)−Mn(1)−N(3)	159.34(12)	N(5)−Mn(2)−N(8)	158.21(14)
O(3)−Mn(1)−O(6)	91.69(11)	O(2)−Mn(2)−N(7)	159.12(12)
N(1)−Mn(1)−N(2)	72.08(12)	O(2)−Mn(2)−O(5)	93.07(11)
N(2)−Mn(1)−N(3)	87.36(12)	N(5)−Mn(2)−N(6)	73.23(14)
N(1)−Mn(1)−N(4)	150.97(12)	N(7)−Mn(2)−N(8)	72.44(14)
N(4)−Mn(1)−O(6)	113.63(12)	Mn(2)−O(5)−P(2)	125.10(17)
O(2)−P(1)−O(3)	112.12(17)	Mn(2)−O(2)−P(1)	133.52(17)
P(1)−O(4)−P(2)	125.85(18)	Mn(1)−O(6)−P(2)	132.91(17)

independent $[Mn(phen)_2]^{2+}$ units bridged by the tetra-anionic pyrophosphate ligand. Pyrophosphate coordinates in a bis-bidentate manner forming two six-membered chelate rings as in **1**.

The N_4O_2 coordination chromophore about each manganese atom is irregular and is derived from four nitrogen atoms from two phen ligands and two oxygen atoms from the bridging pyrophosphate. The best equatorial plane about Mn1 is fined by the [O3−O6−N2−N3] donor set (dihedral angle 40.87°) with Mn(1) displaced 0.013 Å from the mean plane. For Mn(2), the best equatorial plane is defined by the [O2−O5−N6−N7] donor set (dihedral angle 32.36°) with Mn(2) displaced 0.001 Å from the mean plane. The intradimer Mn(1)···Mn(2) distance is 4.700 Å, and the shortest interdimer Mn···Mn distance is 7.842 Å. Both values are shorter than the corresponding ones in **1**. Terminal P═O bonds lengths in the bridging pyrophosphate are 1.504 [P(1)−O(1)] and 1.514 Å [P(2)−O(7)] compared with the inner P−O bond lengths, which range between 1.613 [P(2)−(O4)] and 1.627 Å [P(1)−(O4)]. Key bond lengths and angles for **2** are shown in Table 4. As in **1**, two phen ligands at Mn(1) [N(3)/N(4)] and Mn(2) [N(5)/N(6)] interact with each other via an intramolecular face-to-face $\pi-\pi$ interaction with a separation at closest contact of 3.39 Å, and this interaction flanks the bridging pyrophosphate ligand, (see Figure 3). The phen ligands also interact with adjacent ligands through intermolecular offset face-to-face $\pi-\pi$ interactions, and edge-to-face intermolecular interactions are also evident between some adjacent phen ligands. These interactions form a 2D network (see Figure 4) with the lattice water molecules located between the sheets. These water molecules occupy a potential solvent accessible area of 26.4% of the crystal.[19] The volume occupied by the solvent of crystallization is markedly smaller than that observed for **1** (26.4% compared to 45.7%). This is reflected in the greater density of **2** over **1**, 1.510 vs 1.485 g/cm^3.

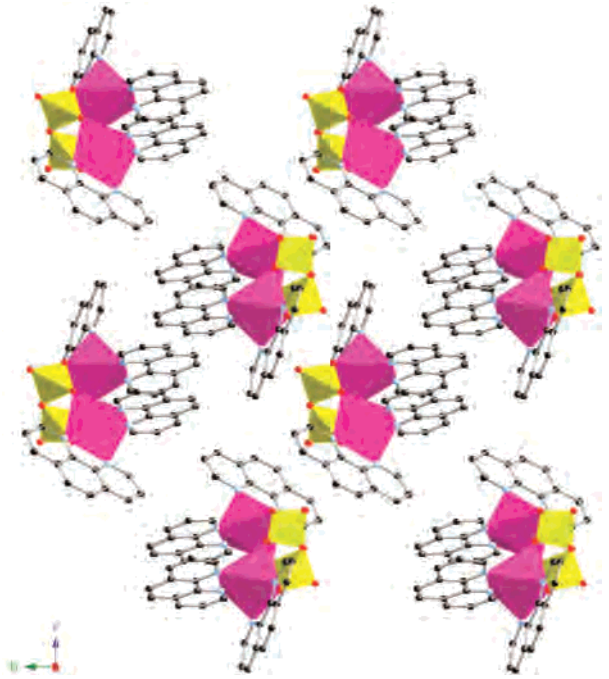

Figure 4. Packing diagram of **2** looking down the crystallographic *a* axis. Note the two-dimensional arrangement of manganese(II) dimers through intra- and intermolecular $\pi-\pi$-type interactions. Hydrogen atoms and lattice waters have been omitted for clarity.

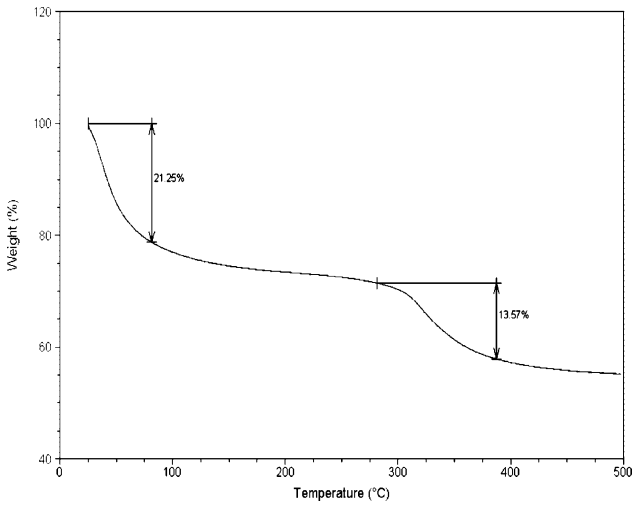

Figure 5. TGA curve of **1** showing immediate loss of 15 water molecules followed by loss of the remaining 12 waters at ca. 280 °C.

Thermal Analysis of 1 and 2. Thermogravimetric analysis (TGA) was performed on powdered samples of **1** (Figure 5) and **2** (Figure S3). The samples were ramped from ca. 25 to 500 °C at a rate of 10 °C/min under nitrogen. The TGA curve for **1** is shown in Figure 5.

The thermal decomposition of **1** shows an inflection at ca. 90 °C in **1** after a mass loss of 21.25%, indicative of the loss of 15 solvent water molecules (Figure 5). The inflection

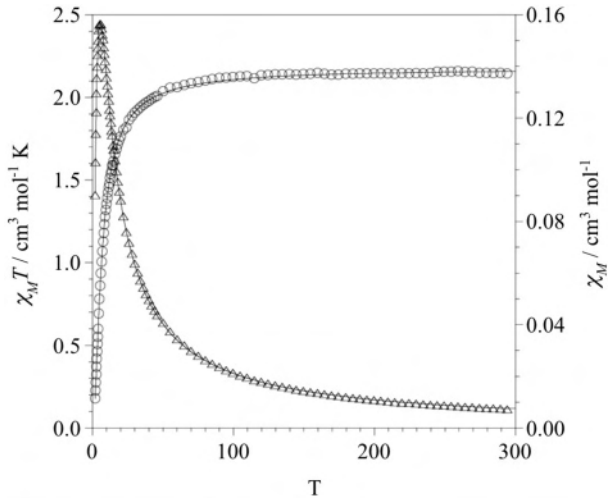

Figure 6. Thermal dependence of χ_M (△) and $\chi_M T$ (○) for **1**. The solid line is the best-fit curve for a nickel(II) dimer with J and g as variable parameters (see text).

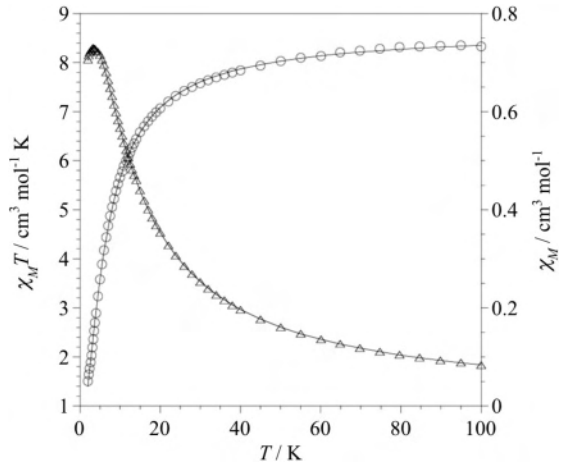

Figure 7. Thermal dependence of χ_M (△) and $\chi_M T$ (○) for **2** at $T \leq 100$ K. The solid line is the best-fit curve for a manganese(II) dimer with J and g as variable parameters (see text).

at ca. 280 °C after a mass loss of 13.57% is equivalent to the loss of the remaining 12 lattice waters. Twelve crystallization water molecules were also noted in the fitting of the elemental analysis after overnight drying in vacuo. This is suggestive of some degree of hydrogen-bonded water network in **1** and/or lattice water being 'buried' within the channels found in **1**.

The TGA curve of **2** shows slight inflection at ca. 50 °C after a mass loss of 6.9%, which is indicative of the removal of five solvent water molecules (Figure S3). The inflection at ca. 75 °C after a mass loss of 3.95% is equivalent to the loss of three water molecules. Decomposition of the dimeric species at ca. 200 °C is consistent with the loss of the remaining water and phen ligands.

Magnetic Behavior of 1 and 2. The magnetic properties of complex **1** in the form of both $\chi_M T$ and χ_M versus T plots [χ_M is the magnetic susceptibility per two Ni(II) ions] are shown in Figure 6. $\chi_M T$ at room temperature is 2.16 cm^3/mol·K, a value which is as expected for two magnetically noninteracting single-ion spin triplets [$\chi_M T = 2.20$ cm^3/mol·K with $g = 2.10$). Upon cooling, this value smoothly decreases until $T = 60$ K and then it exhibits an abrupt decrease and nearly vanishes at very low temperatures. A sharp maximum of the magnetic susceptibility occurs at ca. 5.5 K. These features are typical of a significant antiferromagnetic coupling in **1**. Bearing in mind the dinuclear structure of **1** and the fact that the six-coordinated nickel(II) ion is orbitally nondegenerate, it is possible to represent the intradimer magnetic interaction (J) with the isotropic Hamiltonian $H = -JS_A \cdot S_B$.

The molar magnetic susceptibility for a nickel(II) dimer ($S_A = S_B = 1$) is thus given by eq 1

$$\chi_M = (2N\beta^2 g^2/kT)\{[\exp(J/kT) + 5\exp(3J/kT)]/[1 + 3\exp(J/kT) + 5\exp(3J/kT)\} \quad (1)$$

where N, β, g, and T have their usual meanings and it is assumed that $g_x = g_y = g_z = g$. Although the nickel(II) ion in axial symmetry can have a large zero-field splitting (D), the magnetic behavior of nickel(II) dimers closely follows eq 1 when significant antiferromagnetic coupling occurs. Only in cases where the antiferromagnetic interaction is weak or when the coupling is ferromagnetic is the effect of D relevant to describe the magnetic behavior at low temperatures.[20] This is why in the present case we analyzed the susceptibility data of **1** through eq 1, J and g being the variable parameters. Best-fit values are $J = -3.8$ cm^{-1}, $g = 2.08$, and $R = 1.2 \times 10^{-5}$ (R is the agreement factor defined as $R = \sum_i[(\chi_M)_{obs}(i) - (\chi_M)_{calc}(i)]/\sum_i[(\chi_M)_{obs}(i)]^2$). The calculated curve fits the magnetic data, as shown in Figure 6.

The magnetic properties of complex **2** in the form of both $\chi_M T$ and χ_M versus T plots [χ_M is the magnetic susceptibility per two Mn(II) ions] are shown in Figure 7. The two curves are characteristic of an antiferromagnetic interaction between two single-ion sextuplet spin states: the value of χ_M at room temperature is in the range expected for two $S = 5/2$ states [$\chi_M T = 8.65$ cm^3/mol·K versus the calculated value of 8.75 cm^3/mol·K for two magnetically isolated high-spin Mn(II) ions], increases as the temperature is lowered until a maximum is reached ($T_{max} = 3.5$ K) and finally decreases. In agreement with the dinuclear structure of **2**, its magnetic susceptibility data were analyzed in terms of an isotropic exchange interaction through the Hamiltonian $H = -JS_A \cdot S_B$ ($S_A = S_B = 5/2$) by using eq 2

$$\chi_M = (2N\beta^2 g^2/kT)\{[x + 5x^3 + 14x^6 + 30x^{10} + 55x^{15}]/[1 + 3x + 5x^3 + 7x^6 + 9x^{10} + 11x^{15}]\} \quad (2)$$

with $x = \exp(J/kT)$.

The values of J and g were determined by a least-squares fit minimizing $R = \sum_i[(\chi_M)_{obs}(i) - (\chi_M)_{calc}(i)]/\sum_i[(\chi_M)_{obs}(i)]$.[2] The values obtained were $J = -0.88$ cm^{-1}, $g = 1.99$, and $R = 1.3 \times 10^{-5}$. The calculated curve reproduces well the experimental data over the experimental temperature range.

(20) (a) De Munno, G.; Julve, M.; Lloret, F.; Derory, A. *J. Chem. Soc., Dalton Trans.* **1993**, 1179. (b) Ikotun, O. F.; Ouellette, W.; Doyle, R. P.; Julve, M.; Lloret, F. *Eur. J. Inorg. Chem.* **2007**, *14*, 2083.

Table 5. Selected Magneto-Structural Data for Pyrophosphate-Bridged Dinuclear Metal Complexes

compound	M−O(pyrophosphate)[a] (Å)	d_{M-M}[b] (Å)	$-J$[c] (cm^{-1})	ref
$\{[(bipy)Cu(H_2O)]_2(\mu_4\text{-}P_2O_7)\}\cdot 7H_2O$	1.950	4.646	20	11
$\{[(phen)_4Ni_2(\mu_4\text{-}P_2O_7)]\}\cdot 27H_2O$	2.057	5.031	3.8	this work
$\{[(phen)_4Mn_2(\mu_4\text{-}P_2O_7)]\}\cdot 13H_2O$	2.105	4.700	0.88	this work

[a] Average value for the metal-to-oxygen (bridging pyrophosphate) bond. [b] Metal−metal separation across pyrophosphate. [c] Exchange interaction through bridging pyrophosphate.

Conclusions

The magneto-structural study of the complexes **1** and **2** shows for the first time the ability of the bis-bidentate pyrophosphate ligand to mediate weak but significant antiferromagnetic interactions in homodinuclear species of nickel(II) ($J = -3.8$ cm^{-1}) and manganese(II) ($J = -0.88$ cm^{-1}) ions, which are separated by more than 4.7 Å. In this respect, it deserves to be noted that these results are in line with a somewhat stronger antiferromagnetic interaction which was previously reported for the pyrophosphate-bridged dicopper(II) complex $\{[(bipy)Cu(H_2O)]_2(\mu_4\text{-}P_2O_7)\}\cdot 7H_2O$ (**3**) ($J = -20$ cm^{-1}), where the intradimer metal−metal separation is shorter, ca. 4.646 Å (see Table 5).

The exchange pathway in this family of pyrophosphate-bridged dinuclear complexes is provided by the two M(II)−O−P−O−M(II) arms. In the case of the copper(II) complex, the metal atom has a square pyramidal geometry with two bipy nitrogens and two pyrophosphate oxygen atoms in the basal plane and a water molecule filling the apical position.[11] The unpaired electron on each copper(II) ion is described by a $d_{x^2-y^2}$-type orbital (magnetic orbital), the *x* and *y* axes being roughly defined by the copper-to-pyrophosphate-oxygen bonds. The two magnetic orbitals make a dihedral angle of 58.04°, which is related to the butterfly shape of the bis-bidentate pyrophosphate. The overlap between the magnetic orbitals of the two copper(II) ions through the σ-exchange pathway under these circumstances is predicted to be small, and consequently, a weak magnetic coupling is expected.

In the case of **1** and **2**, the $d_{x^2-y^2}$ magnetic orbital of each metal ion is also defined by the metal-to-pyrophosphate-oxygen bonds, but the occurrence of additional magnetic orbitals [d_{z^2} for nickel(II) and Mn(II) and d_{xy}, d_{xz}, and d_{yz} for Mn(II)] involves the presence of ferromagnetic contributions arising from the interaction between magnetic orbitals of different symmetry, and thus, the antiferromagnetic coupling decreases, as observed.

Acknowledgment. We thank Wayne Ouellette for assistance collecting the X-ray single-crystal data for **1**. Thanks are due to Promega Biotechnology Corporation (Madison, WI), the iLEARN Program, Syracuse University, and the Ministerio Español de Ciencia y Tecnología (Project No. BQU2004-03633) for funding.

Supporting Information Available: Figure S1 shows an alternate view of the packing of **1** along the crystallographic *c* axis. Figure S2 shows the disordered water present in the channels of **1** looking along the crystallographic *c* axis. Figure S3 displays the TGA plot for **2**. Crystallographic information for complexes **1** and **2** are included as a single file containing both CIF files. This material is available free of charge via the Internet at http://pubs.acs.org.

IC700439A